

# A discrete dislocation plasticity study of the micro-cantilever size effect

E. Tarleton,<sup>a</sup> D.S. Balint,<sup>b,\*</sup> J. Gong<sup>a</sup> and A.J. Wilkinson<sup>a</sup>

<sup>a</sup>Department of Materials, University of Oxford, Parks Road, Oxford OX1 3PH UK

<sup>b</sup>Department of Mechanical Engineering, Imperial College London, London SW7 2AZ, UK

Received 16 May 2014; revised 14 November 2014; accepted 18 January 2015

**Abstract**—Micro-cantilevers are increasingly used to extract elastic and plastic material properties through controlled bending using a nanoindenter. Focused Ion Beam milling can be used to produce small scale single crystal cantilevers with cross-sectional dimensions on the order of microns, and electron backscatter diffraction (EBSD) allows cantilevers to be milled from a grain with a desired crystal orientation. Micro-cantilever bending experiments suggest that sufficiently smaller cantilevers are stronger, which is generally believed to be related to the effect of the neutral axis on the evolution of the dislocation structure. A planar model of discrete dislocation plasticity was used to simulate end-loaded cantilevers to interpret the behaviour observed in experiments. The model allowed correlation of the initial dislocation source density and resulting slip band spacing to the experimental load displacement curve. There are similarities between the predictions of this model and those of earlier discrete dislocation plasticity models of pure bending. However, there are notable differences, including a strong source density dependence of the size effect that cannot be explained by geometrically necessary dislocation (GND) arguments, and the effect of the cantilever stress distribution on the locations of soft pile-ups. The planar model was used to identify zero resolved shear stress isolines, rather than the neutral axis, as controlling the soft pile-up location, and source spacing as limiting the slip band spacing in the observed size effect; strengthening was much greater in the source-limited regime. The effect of sample dimensions and dislocation source density were investigated and compared to small scale mechanical tests conducted on titanium and zirconium. The calculations predict a scaling exponent  $n \approx 1$  for the dependence of stress on size if size is normalised by the average source spacing and a term representing the size-independent flow stress is included, whereas the simple power-law form ordinarily used to fit experimental data significantly underestimates  $n$ .

© 2015 Acta Materialia Inc. Published by Elsevier Ltd. This is an open access article under the CC BY license (<http://creativecommons.org/licenses/by/4.0/>).

**Keywords:** Discrete dislocation plasticity; Size effects; Micro-cantilever bending

## 1. Introduction

Micro-pillars and micro-cantilevers do not have a sufficient mobile dislocation density to easily accommodate the imposed plastic strain; this leads to mechanical properties not found in bulk specimens, most notably a size-dependent flow stress, intermittent plastic flow and significant scatter in the response measured from different samples or simulations due to the operation of a small number of dislocation sources. The ‘smaller is stronger’ response has been observed under various loading conditions in a range of metals, semiconductors and ceramics [1], and has been understood in micro-pillars as resulting from truncation of long (low strength) sources [2,3] and dislocation starvation [4,5].

Although the origins of observed dislocation size effects differ, the experimental data are often expressed as  $\log \sigma_f(w)$  vs  $\log w$ , where  $\sigma_f$  is the flow stress and  $w$  a characteristic sample dimension. The data appear to fit a

straight line with gradient  $n$  when plotted in this way, indicating a power law of the form

$$\sigma_f(w) = Aw^{-n} \quad (1)$$

where  $w$  is a characteristic sample dimension and  $A$  is a stress proportionality constant which depends on the boundary conditions and material. Values of the stress exponent reported in the literature vary but are generally in the range  $0.2 < n < 1$  depending on the material and loading conditions [6]. Single crystal micro-pillar compression is the most frequently used geometry and results for a range of fcc materials include: Ni [7] ( $n \approx 0.6$ ), Au [8,9] ( $n \approx 0.6$ ) and Cu [10] ( $n \approx 0.4$ ) and for bcc materials: Mo [11,12] ( $n \approx 0.38$ ), W ( $n \approx 0.21$ ), Ta ( $n \approx 0.41$ ) and Nb ( $n \approx 0.48$ ). [13]. Data for hcp metals are more limited but Sun et al. report ( $n \approx 0.5$ ) for Ti in prism slip [14], while fitting to data in [15] yields  $n \approx 0.8$  for basal slip in Mg compared to  $n \approx 0.4$  from data in [16], again for basal slip, and  $n \approx 0.2$  for pyramidal slip.

Ignoring the data for Mg which shows considerable scatter it is interesting to note that in general  $n^{fcc} > n^{hcp} > n^{bcc}$  whereas the bulk flow stress  $\sigma_0^{bcc} > \sigma_0^{hcp} > \sigma_0^{fcc}$ . This indicates that the different values of  $n$  are possibly an artefact of the experimental data fit to a power law that predicts

\* Corresponding author. Tel.: +44 0 2075 947084; e-mail: [d.balint@imperial.ac.uk](mailto:d.balint@imperial.ac.uk)

$\sigma_f(w) \rightarrow 0$  for large  $w$  whereas, in fact,  $\sigma_f(w) \rightarrow \sigma_0$  for large  $w$ . For materials with low  $\sigma_0$ , Eq. (1) can be used, however in general Eq. (1) will underestimate  $n$ . Furthermore, it will be shown in this paper that for micro-cantilevers the flow stress is also dependent on the dislocation source density and that this dependence can be accounted for by using the form

$$\sigma_f(w) = A(w/w_s)^{-n} + \sigma_0 \quad (2)$$

with  $n \approx 1$ , where  $w_s$  can be thought of as the average source spacing in the material, namely

$$w_s = \frac{1}{\sqrt{\rho_s}} \quad (3)$$

where  $\rho_s$  is the source density. This same scaling law was later found to have been derived independently of this work by Tang et al. [17] using 3D discrete dislocation simulations. The form of Eq. (2) has also been suggested by the work of Korte and Clegg [18] and Dunstan and Bushby [19]. The expression given by Eq. (2) is capable of capturing the source-limited regime in specimen size strengthening. The form in (2) implies that the transition to a source-limited strengthening regime occurs at a smaller sample size when the source density is larger.

Several detailed reviews of the size effect literature have been published [20–22]; for completeness a very brief summary of the most relevant simulation results is included here. 3D discrete dislocation simulations [23,17] of micro-pillars have demonstrated the important role of exhaustion hardening whereby the limited mobile dislocation density produces hardening in addition to forest hardening resulting from dislocation–dislocation interactions [24,25]. The size effect has also been attributed to the limited availability of Frank–Read sources in small sample volumes [26]. For low Frank–Read source densities, sources expand and intersect free surfaces breaking the loop into two segments per source, preventing further plasticity until the stress is sufficiently high to operate one of the arms as a spiral source; this is known as source truncation hardening [27].

Uniaxial compression tests show source density plays a crucial role in the size effect of Au nanopillars [28]. However one large scale ( $0.5 < w < 20 \mu\text{m}$ ) 3D DD study of fcc Ni micro-pillars [23] showed that  $n \approx 0.43$  at  $\rho_s = 10 \mu\text{m}^{-2}$ , which increased to  $n \approx 0.86$  when the source density was decreased to  $0.7 \mu\text{m}^{-2}$ ; some planar discrete dislocation plasticity (DDP) calculations have shown a strong dependence of size effects on source density (e.g. [4,29]).

The stability of dislocation sources has received some attention in the literature. Molecular dynamics calculations have shown that jogs on Lomer–Cottrell dislocations that might form the pinned part of single arm sources are unstable in the high stress loading conditions required to deform Al nano-pillars of diameter 16–50 nm [30], while 3D DDP simulations show the importance of image stresses and cross-slip in controlling the lifetime of intermittent sources which tend to be longer lived in larger diameter samples [31]. However, TEM observations of tensile deformation of Al fibres of diameter 120 nm to  $1.2 \mu\text{m}$  concluded that although operating intermittently, an individual single arm dislocation source is sufficiently stable to generate large plastic strain. Stability of dislocation sources in hcp metals such as Ti and Zr has not received direct attention. 2D DDP simulations have proved useful in examining the size effect

in uniaxial deformation of 2D simulation cells in tension and compression. Deshpande et al. [32] found that the flow strength increases with decreasing specimen size down to a limiting specimen size, at which point the flow strength of the crystals was governed by the nucleation strength of the sources. They performed finite and small strain simulations and found that the main features of size dependence were the same for both analyses. 2D simulations that incorporate a larger set of constitutive rules for short range interactions to account for 3D effects such as line tension, junction formation and destruction, and dynamic source and obstacle creation have been developed by Benzerga and colleagues [33,34]. Their work emphasised the importance of the length of sources on the observed size effects. The stress required to initiate plastic flow in a larger sample was reduced as the source length was larger and hence easier to operate. In contrast, 3D simulations have since found that the size dependence of the plastic response is independent of source strength [17]. Cu micro-pillar compression experiments showing that the size exponent  $n$  increases from  $\approx 0.2$  at low (2–5%) strain to  $\approx 0.45$  at high (20–30%) strain have been successfully simulated using a 2D DDP model [35]. This could explain the variation in reported values of  $n$  in the literature.

The size effect when a strain gradient is present has often been attributed to geometrically necessary dislocations (GNDs) [36–38]. However, these studies ignore other changes that occur as the physical dimensions are decreased, such as the reduced availability of sources. DDP simulations have provided useful insights into the size effect in pure bending: the formation of soft pile-ups at the neutral axis [39] was found to cause source shutdown and associated strengthening, consistent with prior 2D simulations of pure bending [40] where strengthening was understood in terms of GNDs. In this work we focus on the origins of specimen size strengthening in micro-cantilevers, and in particular, the source-limited regime, for the purpose of interpreting micro-cantilever bending experiments carried out on hcp materials.

## 2. Model

A plane strain, quasi-static discrete dislocation plasticity formulation was used to simulate elastic/plastic micro-cantilever bending of a hcp single crystal. Elastic isotropy and small strain conditions were assumed. The plane of the simulation was specified by the  $x_1 - x_2$  axes in Fig. 1. Dislocation glide only on the  $\langle a \rangle$  prismatic slip systems, with  $\{10\bar{1}0\}$  slip plane normals and  $\langle 11\bar{2}0 \rangle$  slip directions as depicted in Fig. 1(a), was considered. The low stacking fault energy in hcp materials such as Zr and Ti means there is minimal cross slip [1], which is not included in the formulation. In this orientation basal planes are parallel to the plane of the beam, as illustrated in Fig. 1(b). Slip plane normals and slip directions, given by:

$$\mathbf{m} = [\cos(\lambda + \theta), \sin(\lambda + \theta), 0] \quad (4)$$

$$\mathbf{n} = [-\sin(\lambda + \theta), \cos(\lambda + \theta), 0] \quad (5)$$

have zero out-of-plane components, hence an arbitrary set of slips on these systems satisfies the conditions for plane strain deformation:  $\varepsilon_{13} = \varepsilon_{23} = \varepsilon_{33} = 0$ . The reference orientation for the slip directions is  $\lambda = (0, 60^\circ, 120^\circ)$  relative to the reference  $x_1$ -axis shown in Fig. 1(a). Unless otherwise

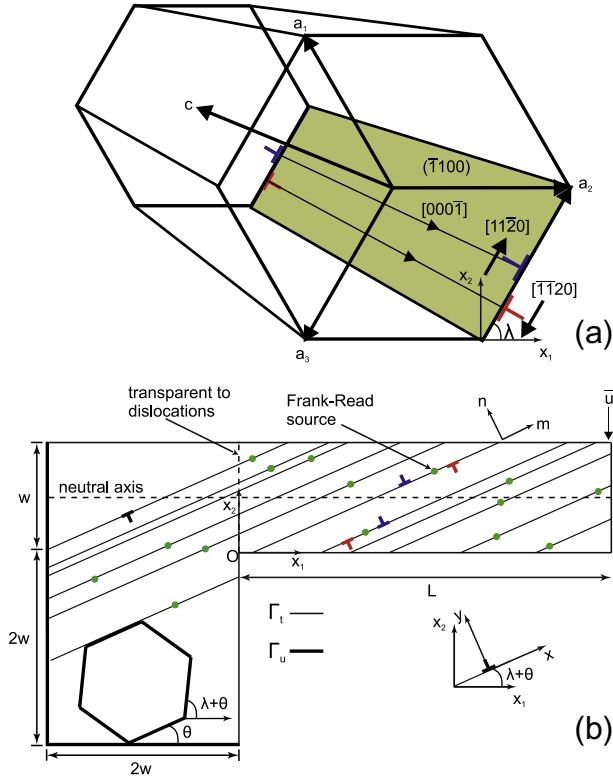


**Fig. 1.** Schematic illustrations of (a) an  $\langle a \rangle$  prismatic slip system in an hcp material and (b) the model geometry which contains the three  $\langle a \rangle$  prismatic slip systems; only one is shown for simplicity.

noted, the crystal is oriented by a counterclockwise  $\theta = 45^\circ$  rotation about the  $c$ -axis, which orients the slip directions at  $(45^\circ, 105^\circ, 165^\circ)$  relative to the longitudinal beam axis and causes slip to predominate on the  $45^\circ$  system because the resolved shear stress on that system is the greatest.

We follow the formulation developed by Van der Giesen and Needleman [41], which utilises the superposition principle of Lubarda et al. [42] to enforce the desired traction and displacement boundary values. Field quantities in the domain are partitioned as

$$u = \tilde{u} + \hat{u}$$

$$\varepsilon = \tilde{\varepsilon} + \hat{\varepsilon} \quad (6)$$

$$\sigma = \tilde{\sigma} + \hat{\sigma}$$

where the  $(\tilde{\phantom{x}})$  fields are the superposition of the infinite plane analytical fields of all edge dislocations in the body and the  $(\hat{\phantom{x}})$  fields satisfy the modified boundary value problem

$$\nabla \cdot \hat{\sigma} = 0$$

$$\hat{\sigma} = \mathbf{L} \hat{\varepsilon} \quad (7)$$

$$\hat{\varepsilon} = \frac{1}{2} \left( \nabla \hat{u} + (\nabla \hat{u})^T \right)$$

where  $\mathbf{L}$  is the fourth order tensor of elastic constants, and

$$\hat{\sigma} \cdot \mathbf{n} = \bar{\mathbf{t}} - \tilde{\sigma} \cdot \mathbf{n} \quad \text{on } \Gamma_t$$

$$\hat{u} = \bar{u} - \tilde{u} \quad \text{on } \Gamma_u \quad (8)$$

where  $\mathbf{n}$  is the outward pointing unit normal, and  $\Gamma_t$  and  $\Gamma_u$  are the parts of the boundary over which tractions and displacements are applied, respectively; the  $(\hat{\phantom{x}})$  problem is usually solved by the finite element method. In the micro-cantilever problem,  $\bar{\mathbf{t}} = 0$  on the free edges and  $\bar{\mathbf{u}} = 0$  on the fixed edges, with  $\bar{t}_1 = 0$  and  $\bar{u}_2 = iut$  at the single end loaded node depicted in Fig. 1(b).

The glide component of the Peach–Koehler force on dislocation  $i$  is

$$f^i = \mathbf{n}^i \cdot \left( \hat{\sigma} + \sum_{j \neq i} \tilde{\sigma}^j \right) \cdot \mathbf{b}^i \quad (9)$$

where  $\mathbf{n}^i$  is the slip plane normal and  $\mathbf{b}^i$  the Burgers vector for the  $i$ th dislocation, and the stress field for every dislocation  $\tilde{\sigma}^j$  is calculated analytically using the stress tensor for a straight edge segment of infinite length in an infinite domain. The micro-cantilevers are assumed to be initially free of mobile dislocations. Dislocations are nucleated as dipoles originating from Frank-Read sources, where in three dimensions the plane of the simulation is perpendicular to a source's trapped dislocation line and cuts the incipient dislocation loop through its purely edge segments, as depicted in Fig. 2. A dipole is nucleated with a spacing

$$L_{nuc} = \frac{\mu b}{2\pi(1-\nu)\tau_{nuc}} \quad (10)$$

where  $\mu$  is shear modulus,  $\nu$  is Poisson's ratio and  $b$  is the Burgers vector, when the resolved shear stress acting on it equals or exceeds the nucleation stress  $\tau_{nuc}$  for a duration  $t_{nuc}$ . At this spacing the resolved shear stress exerted by one of the dislocations in the dipole on the other is exactly balanced by  $\tau_{nuc}$ . Sources are distributed randomly throughout the crystal on slip planes spaced a distance  $r_{plane}$  apart. Source strengths are chosen randomly from a normal distribution with an average value  $\tau_{nuc}$  and a standard deviation that represents the statistical distribution of trapped dislocation line lengths in the material. Furthermore, we assume that the dislocation source density is constant throughout the simulation. Dislocations move assuming zero Peierls stress according to a linear mobility law

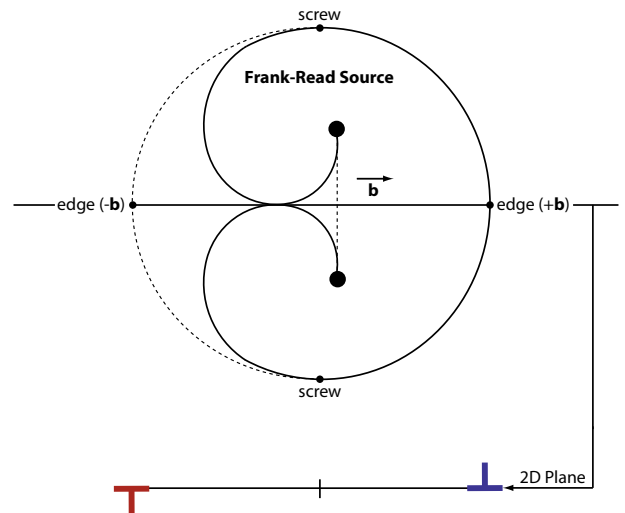


**Fig. 2.** Planar representation of a Frank-Read source.

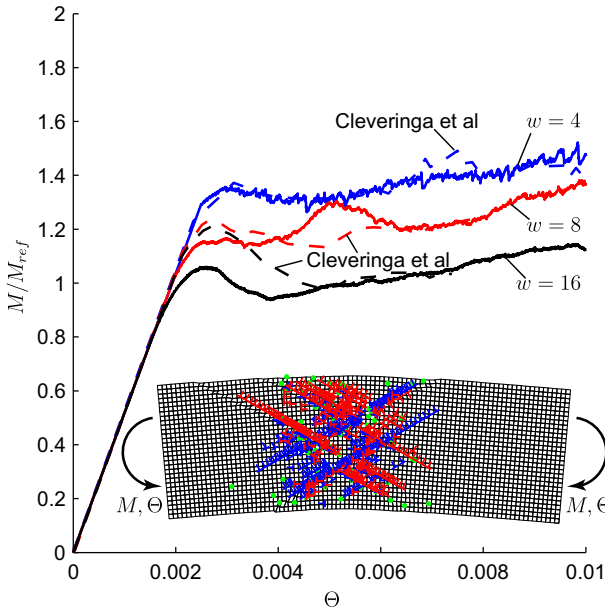


**Fig. 3.** Comparison of this code with results published by Cleveringa et al. [40]. The inset shows the deformed mesh at the end of the simulation with the dislocation structure and active sources superimposed for  $w = 4$ .

$$v^i = \frac{f^i}{B} \quad (11)$$

where  $v^i$  is the velocity of the  $i$ th dislocation and  $B$  is a drag coefficient. Point obstacles with strength  $\tau_{obs}$  and density  $\rho_{obs}$  are distributed randomly throughout the crystal on the slip planes. Dislocations are pinned by obstacles, but released if the resolved shear stress on the obstacle equals or exceeds  $\tau_{obs}$ . Dislocations are also pinned if they reach  $r_c = 5b$  of  $\Gamma_u$ , although this rarely occurs in practice as the base size,  $2w$ , is large enough to prevent a significant number of dislocations reaching  $\Gamma_u$ , since the resolved shear stress on a dislocation in the base becomes very low as it approaches  $\Gamma_u$ . Dislocations of opposite sign annihilate when their spacing is less than or equal to  $5b$ , by moving them to a common midpoint and removing them from the simulation. Dislocations may exit at free surfaces; a description of how this is handled is given in Appendix A.

The (^) problem was solved using the finite element method with four node bi-linear elements with 4 integration points and a uniform grid mesh with 120 elements along the beam length and 7500 elements in total, which was found to give a convergent solution and accurately resolve the (~) part of the boundary conditions for all specimen sizes.

### 2.1. Code validation

The simulations reported here were performed using a new discrete dislocation plasticity code written in Matlab, therefore comparison was made with simulations reported in the literature for tension [4] and pure bending [40] to validate the implementation.<sup>1</sup> The pure bending comparison is shown in Fig. 3; the parameters used in our pure bending

calculation were identical to those used in [40]. In both cases good agreement was found in both the dislocation structure and load–displacement response of the material. The differences between our simulations and those in [40] are within the range of expected statistical scatter when repeating the same discrete dislocation plasticity simulation using identical parameters.

### 3. Experiments

The experiments were designed to ensure that the active slip systems could be simulated using planar discrete dislocation plasticity. Grade 1 (commercially pure) CP-Ti (supplied by Timet) and CP-Zr (from Goodfellow), both of which have the hexagonal crystal structure ( $\alpha$ -phase) at room temperature, were selected for the micro-cantilever tests. The raw materials were first annealed in vacuum at a temperature just below their  $\alpha$ -to- $\beta$  transition for at least 24 h to reduce the density of residual lattice defects, e.g. dislocations and then cooled down to room temperature in a vacuum oven. After the heat treatment, all specimens were ground using 2500 grit paper and carefully polished using colloidal silica. Polarized light optical microscopy and electron backscatter diffraction (EBSD) were performed to map the grain and crystal orientations. Grains with the orientation shown in Fig. 1 were selected. Single-crystal micro-cantilevers were prepared so that the crystal orientation exactly matches that of the model as shown in Fig. 1.

All micro-cantilevers were milled using a Focused Ion Beam (FIB) platform. Surfaces were polished down to 40 pA at 30 kV to minimise the FIB damage. The cantilevers were milled with a triangular cross-section so that they could be prepared at any site on the polished surface. The width of the micro-cantilevers varied from 1 to 10  $\mu\text{m}$ . The length to thickness ratio was 6 : 1 for all sizes. Fig. 4 shows a 5  $\mu\text{m}$  wide cantilever after testing. It is important to obtain accurate beam dimensions as the response of the beam is governed by the cube of the aspect ratio, hence the dimensions of all cantilevers were measured via a high resolution field emission gun scanning electron microscope

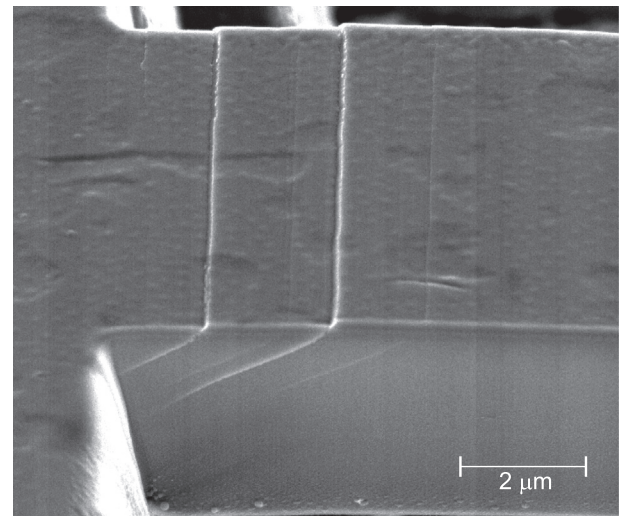


**Fig. 4.** SEM image of the fixed end of a  $w = 5 \mu\text{m}$  Ti cantilever showing slip steps at the free surface produced by slip bands with a spacing of approximately 2  $\mu\text{m}$  at  $\varepsilon = 0.01$ .

<sup>1</sup>In order to achieve traction free top and bottom edges in pure bending,  $\sigma_{22}^{(1)} = -\sigma_{22}$  and  $\sigma_{22}^{(2)} = 0$  are required on  $x_2 = 0$  and  $w$ , rather than the conditions given in Eqs. (15) and (17) in [40].



(FEG-SEM). The micro-cantilever tests were conducted using a NanoXP nano-indentation system. A nano-positioning stage is integrated in this system, which enables an atomic force microscope (AFM) scan of a cantilever prior to testing. The deflection of the cantilever can then be accurately determined based on the AFM image. While the nano-indenter is basically a load control device, using fast feedback our micro-cantilever tests were conducted under the same constant displacement rate as in the simulations.

#### 4. Comparison with experiments

Simulations were performed using the parameters shown in Table 1. Previous work on Ti [43] used crystal plasticity finite element analysis to infer a critical resolved shear stress value for an infinitely large sample. Trial simulations for large cantilevers were used to establish a corresponding combination of mean and standard deviation in nucleation stress, source density, and obstacle density and strength. The time step must be sufficiently less than the nucleation time, however an adaptive time step was found to significantly reduce the computational time without affecting the results. Velocity correction algorithms were used to ensure that dislocations do not overshoot neighbouring dislocations or obstacles, and to mitigate positional vibrations. The computational parameters were defined following convergence studies to ensure the results were independent of the adaptive time step parameters  $\Delta t_{min}$  and  $\Delta t_{max}$ , loading rate  $\dot{u}/L$ , dislocation core cut-off distance  $r_c$ , slip plane spacing  $r_{plane}$ , maximum dislocation velocity  $v_{max}$  and number of elements  $N_{elements}$ .

The source density  $\rho_s$ , standard deviation of the source strength and the drag coefficient  $B$  were fitted to the largest

Ti beam. The obstacles were assumed to have a constant strength of  $3\tau_{nuc}$  as in other planar discrete dislocation plasticity studies, with a density of  $10\rho_s$ . Obstacles were found to have only a weak influence on the overall load–displacement curves, because large shear stresses resulting from pile-ups at obstacles allow them to be overcome. A lower value of  $\rho_{obs}$  could be used if a larger value of  $B$  was used as they both act to reduce the dislocation mobility and consequently increase the flow stress. If the obstacles had a finite size and induced a stress field then they could have a more significant effect on the plastic response. The standard deviation of the source strength shown in Table 1 was found to provide a smooth transition from elastic to plastic response; a sudden drop in flow stress would occur at the elastic limit if a uniform source strength were used, but the same flow stress would be reached after further straining. The source density obtained by fitting was later observed to predict a slip band spacing consistent with the slip traces clearly visible in the SEM images, providing further justification that  $\rho_s = 5 \mu\text{m}^{-2}$  is reasonable for these cantilevers. A value of  $B = 10^{-4} \text{ Pa s}$  is typically used for aluminium [40,4], hence the value of  $B = 4 \times 10^{-4} \text{ Pa s}$  used here for Ti and Zr is also reasonable.

The experiments were performed on beams with a triangular cross section whereas the model assumes a rectangular cross section with unit thickness  $d$ . The load displacement response can be converted to a non-dimensional form to allow comparison across different beam sizes and cross sectional shapes by the following:

$$I^{sim} = \frac{dw^3}{12}, \quad I^{exp} = \frac{dw^3}{36} = \frac{I^{sim}}{3} \quad (12)$$

$$\sigma^{sim} = \frac{FLw}{2I^{sim}}, \quad \sigma^{exp} = \frac{FLw}{2I^{sim}/3} = 3\sigma^{sim} \quad (13)$$

$$\varepsilon^{sim} = \frac{3w}{2L^2} u^{sim}, \quad \varepsilon^{exp} = 3\varepsilon^{sim}. \quad (14)$$

The stress and strain vary throughout the beam but the above represent the maximum values at the fixed end at the free surface.

A comparison of the discrete dislocation plasticity predictions and the experiments for the Ti and Zr micro-cantilevers are shown in Figs. 5 and 6, respectively, which show stress vs strain at the fixed end at the free surface; two repeats were done for each size, as in the experiments. The same parameters were used in the simulations for Ti and Zr apart from the elastic constants and the Burgers vector (see Table 1). The model reproduced the measured load–deflection response, and consequently the stress vs strain curves, although the yield point was slightly higher in the simulation than the experiment for the  $10 \mu\text{m}$  Ti beam. The model accurately reproduced the observed increase in flow stress and hardening with decreasing beam size.

The deformed mesh ( $\times 10$  displacement scaling factor applied) for a  $w = 5 \mu\text{m}$  Ti cantilever at the end of the simulation ( $\varepsilon = 0.01$ , or  $u_2 = -1.2 \mu\text{m}$ ) is shown in Fig. 7 for the  $\theta = 45^\circ$  case. The sense (and approximate spacing) of the slip steps formed by dislocations exiting at the free surface are in agreement with those observed in the experiments as illustrated in Fig. 4, providing further justification that the plane strain assumption is appropriate in this case.

**Table 1.** Model parameters used unless stated otherwise.

	$\mu$ (GPa)	$\nu$	$b$ (nm)
Ti	39.5	0.33	0.295
Zr	37.1	0.32	0.323
Sources	$\rho_s$ ( $\mu\text{m}^{-2}$ )	$\tau_{nuc}$ (MPa)	std (MPa)
	5	110	20
Obstacles	$\rho_{obs}$ ( $\mu\text{m}^{-2}$ )	$\tau_{obs}$ (MPa)	std (MPa)
	50	330	0
Computational	$\Delta t_{min}$ (ns)	$\Delta t_{max}$ (ns)	$\dot{u}/L$ ( $\text{s}^{-1}$ )
	0.5	5	$10^3$
	$r_c$ (b)	$r_{plane}$ (b)	$v_{max}$ ( $\text{ms}^{-1}$ )
	5	30	20
	$N_{elements}$ 7500		
Slip systems	$N_{systems}$	$\lambda$	$\theta$
	3	$60^\circ$	$45^\circ$
Geometry	$w_{base}/w$	$L/w$	
	2	6	
Material	$B$ (Pa s)	$t_{nuc}$ (ns)	
	$4 \times 10^{-4}$	10	

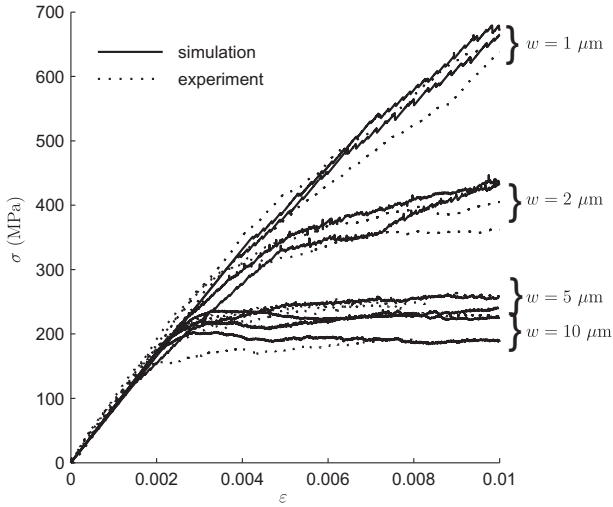


**Fig. 5.** Simulated and experimental response of titanium 6:1 cantilevers for beam widths  $w = 1, 2, 5$  and  $10 \mu\text{m}$ .

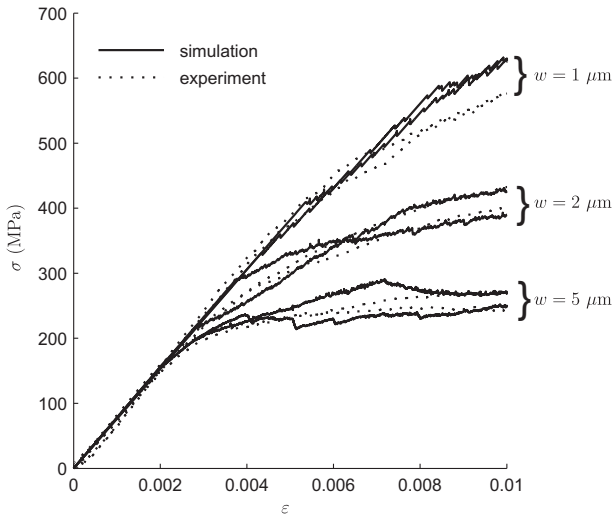


**Fig. 6.** Simulated and experimental response of zirconium 6:1 cantilevers for beam widths  $w = 1, 2$  and  $5 \mu\text{m}$ .

Experiments were also performed for the  $\theta = 0^\circ$  orientation (symmetric slip), and the flow stress was found to increase by approximately 15% compared to the  $\theta = 45^\circ$  orientation (predominantly single slip) due to the reduced Schmidt factor in the former, as shown in Fig. 8 with accompanying simulation results. As three slip systems are available in the  $\theta = 0^\circ$  orientation, the first dipole is nucleated when  $\max_i |\tau(\theta + \lambda_i)| = \tau_{nuc}$ , where  $i$  is the slip system number, which can be estimated analytically using (15); the resolved shear stress on a plane with orientation  $\theta + \lambda$  based on the elasticity solution for small strain, linear isotropic elastic end-loaded cantilever bending is:

$$\tau = \frac{F}{2I} ((L - x_1)(w/2 - x_2) \sin(2(\theta + \lambda)) - x_2(w - x_2) \cos(2(\theta + \lambda))). \quad (15)$$

At a crystal rotation  $\theta = 15^\circ$ , the resolved shear stress,  $\tau$ , on the third slip system, which is at an angle  $\theta + \lambda_3 = 135^\circ$ , is maximised;  $\theta = -15^\circ$  would maximise  $\tau$  on the second

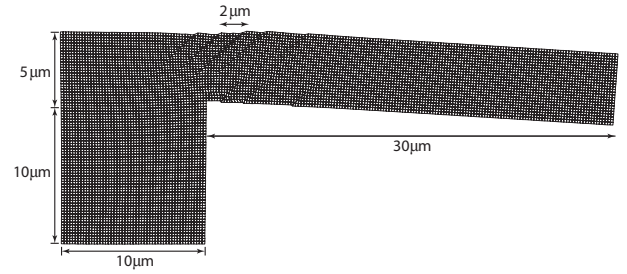


**Fig. 7.** Deformed mesh and slip band spacing for the  $w = 5 \mu\text{m}$  Ti beam.

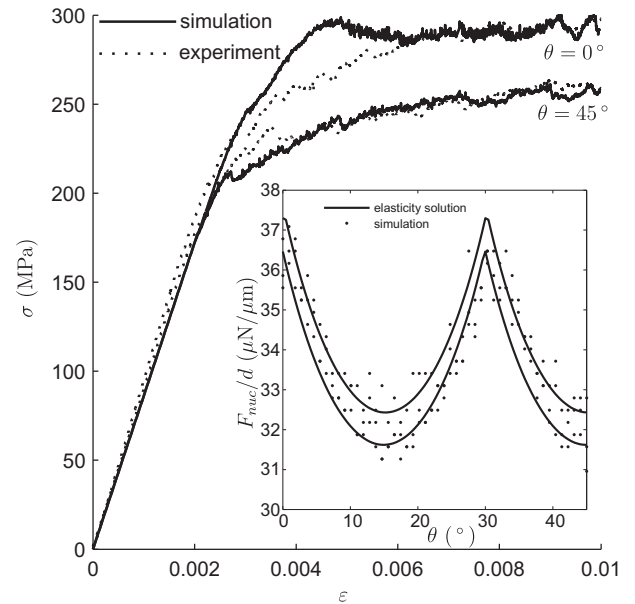


**Fig. 8.** The influence of crystal rotation for the  $w = 5 \mu\text{m}$ ,  $L = 30 \mu\text{m}$  Ti beam; experiments for  $\theta = 0^\circ$  and  $\theta = 45^\circ$  are compared to the simulations. The inset shows the force per unit thickness required to nucleate the first dipole as a function of the slip plane angle with three simulations performed for each angle, and the analytical prediction for the upper free surface (upper solid curve), and lower free surface (lower solid curve).

system. A crystal rotation  $\theta = 30^\circ$  is equivalent to  $\theta = 0^\circ$ , in that there are two active symmetric systems with a Schmidt factor of  $\pm 0.433$ . Simulations were performed to investigate the influence of the orientation angle by examining the applied force required to nucleate the first dipole. A high source density  $\rho_s = 100 \mu\text{m}^{-2}$  with zero standard deviation in source strength was used to minimise scatter. Based on the elasticity solution for end-loaded cantilever bending, the highest stresses should occur at the free surfaces of the built-in end, i.e.  $x_1 = 0$  with  $x_2 = 0$  or  $x_2 = w$ . In the simulations, the first dipole was found to nucleate at  $x_1 \approx 0$  with  $x_2 \approx 0$  or  $x_2 \approx w$ . Due to the presence of the base in the simulations (and experiments), the stress fields are not perfectly symmetric with respect to the neutral axis as predicted by the elasticity solution, therefore sources near the lower free surface at the built-in end were more likely to nucleate. The force at which nucleation first occurred was found to be in good agreement with that predicted analytically for the full range of crystal rotations, and the experimental results for  $\theta = 0^\circ$  and  $\theta = 45^\circ$ , as shown in the inset in Fig. 8; an

increase in the flow stress of  $\approx 15\%$  for  $\theta = 0^\circ$  relative to  $\theta = 45^\circ$  was observed in the simulations, in agreement with the experiments.

### 5. Interpretation of the micro-cantilever size effect

As pointed out by Nye [44] and Ashby [45], plastic bending requires GNDs. Cleveringa et al. found that the size effect in pure bending is dominated by geometrically necessary dislocations (GNDs) [40], and noted that the number of GNDs scales with beam size for a fixed plastic curvature. The slip plane length, hence number of dislocations that can fit on a slip plane also scales with beam size. This implies that the number of slip bands is independent of the beam size, which means that the slip band spacing scales linearly with beam size; the slip band spacing should also decrease with increasing plastic curvature, provided sources are available to create new GNDs. The implication is that strengthening can be expected for sufficiently small beams, when the slip band spacing is such that the stress fields of dislocations on adjacent slip bands begin to interact. Recent experimental [43] and three-dimensional discrete dislocation plasticity analyses [39] of micro-cantilever bending interpreted the size effect primarily in terms of ‘soft pile-ups’ occurring at the beam neutral axis. The GND and soft pile-up interpretations are similar, although the latter considers that GNDs, which are immobile by definition, are not in general available wherever required; they must originate from lowest strength sources in regions of locally high stress and glide to locations where the resolved shear stress is zero, thereby achieving the applied plastic strain gradient. Hence the soft pile-up interpretation implies that details of the source structure might play an important role in the micro-cantilever size effect.

The point sources were randomly distributed among the slip planes of the three  $\langle a \rangle$  prismatic slip systems. When the sample dimensions are reduced to a multiple of the source spacing, only a small number of sources are present in the high stress region (near the upper and lower free surfaces at the fixed end). The exact position of the sources in this region, which we will refer to as the source structure, dictates the plastic response of the material. This is also what leads to the scatter in the simulations and in experiments.

Under bending, dislocation dipoles nucleate in the most highly stressed regions near the free surfaces, which are localised at the built-in end in the case of a cantilever. Considering slip planes oriented by an acute counter-clockwise angle relative to the beam axis, resolved shear stress is negative in the upper half of the beam, and positive in the lower half for a positive end rotation in pure bending, or for a downward end load in cantilever bending; the opposite is true when the slip plane orientation angle is obtuse. Hence  $-b$  dislocations escape at the free surface and  $+b$  dislocations are driven towards the interior of the beam on acutely oriented planes, and the opposite happens on obtusely oriented planes. This is depicted schematically in Fig. 1(b), and is observed for the simulations of pure bending in Fig. 3 and cantilever bending in Fig. 9. Although the first slip system was the most active, some plasticity does occur on the second and third slip systems, indicated by the  $-b$  (red) dislocations in Fig. 9.

When a source first nucleates a dipole, the inner (with respect to the neutral axis) dislocation glides on its plane to the location of zero resolved shear stress and stops.

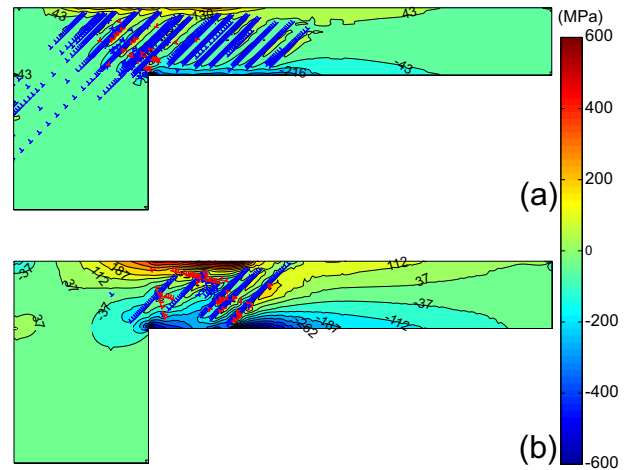


Fig. 9.  $\sigma_{11} = \hat{\sigma}_{11} + \tilde{\sigma}_{11}$  and the dislocation structure for (a)  $w = 9 \mu\text{m}$  and (b)  $w = 3 \mu\text{m}$  at  $\varepsilon = 0.01$ .

Further nucleations from the same source give rise to a soft pile-up, in that the location of zero resolved shear stress on the lead dislocation is altered by those behind it, hence the lead dislocation is effectively pushed to a new stationary position. The stationary position of the lead dislocation, i.e. the soft pile-up location, is that which allows the ensemble of dislocations to achieve the applied plastic strain gradient.

Back stress from a soft pile-up makes it harder to reactivate the source from which the dislocations originated. For a cantilever beam of a given size, this causes hardening and eventually leads to the nucleation of dislocations on neighbouring slip planes that are under a state of lower resolved shear stress because of the highly localised nature of the stresses in cantilever bending; this is fundamentally different from pure bending, where the stress state does not vary along the length of the beam. The effect is modulated by the statistics of the positions and strengths of Frank-Read sources on the available slip planes. Soft pile-up length scales with the beam size, hence by this reasoning sufficiently smaller beams should exhibit greater hardening, and have a higher flow stress under end-loaded cantilever bending, as observed in Figs. 5 and 6.

Two important insights arise from a soft pile-up interpretation of cantilever bending. (i) The locations and operation of the soft pile-ups differ in cantilever bending and pure bending. Hence a pure bending interpretation of size-dependent strengthening in cantilever bending does not reveal the full behaviour. (ii) The ability of the material to satisfy geometrical necessity depends upon the available sources. Or in other words, the applied load required to achieve a given plastic strain gradient can be strongly dependent upon the source structure. These factors will be explored in greater detail in the next two sub-sections.

#### 5.1. Soft pile-up locations

In pure bending, the soft pile-up locations are at the neutral axis and do not depend on the slip plane angle, because of the absence of shear stress with respect to the natural beam axes. In cantilever bending, the soft pile-up locations depend on the slip plane angle. To illustrate this, zero resolved shear stress (see Eq. (15)) isolines for a single slip plane oriented by a counter-clockwise angle  $\theta$  relative to the

beam axis under end-loaded cantilever bending are shown in Fig. 10 for a beam aspect ratio  $L/w = 5$ . The soft pile-up length, which affects both hardening and flow stress, depends on the slip plane angle and does not, in general, coincide with the neutral axis. Although it may be observed by making Eq. (15) dimensionless that as  $w/L \rightarrow 0$ , the zero isoline of resolved shear stress for any slip plane angle moves towards the neutral axis and becomes independent of slip plane angle, which is the very slender beam limit.

As seen in Fig. 10, as the slip plane angle approaches  $0^\circ$ , the zero resolved shear stress isoline approaches the lower free surface; it approaches the upper free surface as the slip plane angle approaches  $90^\circ$ . This could be important, particularly for single-slip situations as in the experiments: although the resolved shear stress on such a plane is relatively low, if it is active the soft pile-up could push through the free surface, thereby creating a channel of easy slip by continuous source activation. This was observed in the simulations.

Active slip planes that are nearly horizontal or vertical tend to fill by continuous activation of a source on the long side of the soft pile-up, whereas active slip planes oriented at  $45^\circ$  tend to fill by activation of two sources on the same plane in the high stress near-surface regions, rather than a single soft pile-up pushing through the neutral axis to the opposing free surface.

Thin elastic boundary layers of high stress near the free surfaces are evident in Fig. 9. On a slip plane, the active source that is nearest to the free surface loses its  $-b$  dislocations to the free surface (for a positive plane orientation), leaving a dislocation-free (denuded) region between the source and the free surface. The average size of the denuded zone is a fixed multiple of  $1/\sqrt{\rho_s}$ , hence it is independent of beam size and therefore a linearly increasing fraction of the beam height for decreasing beam size. This is evident for the two beam sizes depicted in Fig. 9. Denuded zones were also observed for pure bending by Cleveringa et al. [40], and in recent three-dimensional simulations of pure-bending (e.g. [39]). This is a strengthening effect in addition to that resulting from slip band interaction for sufficiently small beam sizes; the denuded zones increase load as a result of the increasing fraction of elastic bending occurring near the free surfaces, and the corresponding reduction in the soft pile-up length.

## 5.2. Source-limited strengthening

As previously noted, the plastic strain gradient in bending requires geometrically necessary dislocations that must nucleate from the available sources. Hence a source-limited regime of strengthening should exist when the beam size is sufficiently small that the slip band spacing is on the order of  $1/\sqrt{\rho_s}$  (a GND interpretation of size-dependent

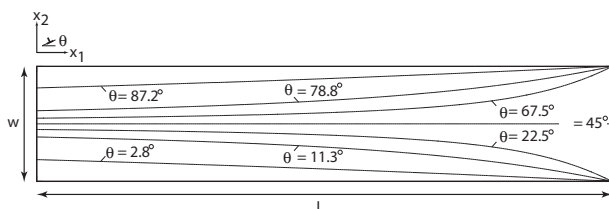


Fig. 10. Zero resolved shear stress isolines for different slip plane angles.

strengthening implies that slip band spacing decreases linearly with decreasing beam size), although the exact onset of source-limited strengthening can be strongly affected by the statistics of the source population in the region of high stress in the beam. A lack of sufficient sources can greatly enhance the observed strengthening for very small beams. To illustrate this, flow stress  $\sigma_f$  is plotted vs source density  $\rho_s$  for different beam sizes in Fig. 11. A total of 63 simulations were performed with different source structures for each source density (21 for each of the three beam sizes), with average value fits to the respective data sets given by the solid lines. Considerable strengthening is evident for small fixed beam sizes at low source densities, and the onset of the source-limited regime occurs at larger source densities for smaller beams. The  $1 \mu\text{m}$  beam is source-limited for the entire range of source densities considered in Fig. 11, and all beam sizes tested experimentally ( $1 \leq w \leq 5 \mu\text{m}$ ) are source limited according to the source density obtained by calibration to the experimental data,  $\rho_s = 5 \mu\text{m}^{-2}$ , which corresponds to  $1/\sqrt{\rho_s} \approx 0.45 \mu\text{m}$ . The amount of strengthening resulting from source limitation can equal or exceed that achieved by the GND strengthening mechanism alone. This indicates that the source density as well as the statistics of the source structure play a crucial role in the size effect for very small beam sizes, such as those used in the micro-cantilever experiments in this study. It is therefore the combination of soft pile-ups and source limitation that produces the observed size effect in the micro-cantilevers.

To explore this further, simulations were performed to identify the relationships between source density, slip band spacing and beam size. The results are shown in Fig. 12, with average value fits given by the solid lines. The simulations were performed for beams with a constant aspect ratio  $L/w = 6$ . To elucidate the trend, higher source densities of  $\rho_s = 15 \mu\text{m}^{-2}$  and  $45 \mu\text{m}^{-2}$  were simulated in addition to the value  $\rho_s = 5 \mu\text{m}^{-2}$  found by calibration to the experimental data, which reduce the scatter in the response. In all cases the standard deviation of the source strength distribution was set to zero, also to reduce the scatter in

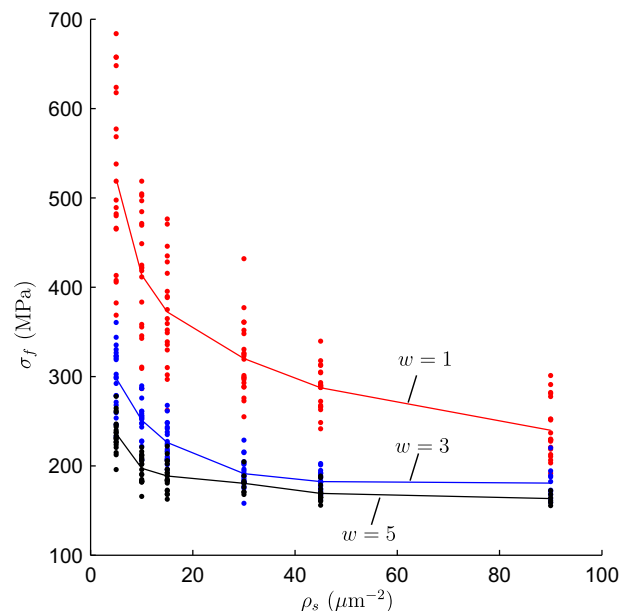


Fig. 11. Flow stress vs source density for three different beam sizes.



the response. No obstacles were used to reduce the computation time. Slip band spacing  $\Lambda$  was defined as the average distance between adjacent active slip planes. A slip plane was considered active if it had  $m \times w$  or more dislocations on it, where  $m$  is a specified integer value. This corresponds to a threshold density of dislocations on a slip plane that is invariant with respect to beam size. The results shown in Fig. 12 are for  $m = 5$ . The slip band spacing was not very sensitive to the choice of  $m$  in the range  $1 \leq m \leq 10$ . A total of 63 simulations were performed with different source structures for each beam size (21 for each of the three source densities). The red, blue and black solid lines in Fig. 12 are the averages of the respective sets of 21 simulations for the  $5 \mu\text{m}^{-2}$ ,  $15 \mu\text{m}^{-2}$  and  $45 \mu\text{m}^{-2}$  source densities. The horizontal dotted lines are the respective approximate threshold values ( $1/\sqrt{\rho_s}$ ) for the source-limited regime.

It can be observed, particularly for the larger source densities which reduce the scatter in the response, that there is a linear scaling of slip band spacing with beam size. This is consistent with the geometrically necessary dislocation argument presented by Cleveringa et al. [40] that says the number of slip planes is independent of beam size, which implies that slip plane spacing scales linearly with beam size. This demonstrates that GNDs dominate the size effect in micro-cantilever bending as in pure bending, but only for the larger beam sizes; as shown in Fig. 11, smaller beams are source-limited and both mechanisms make significant contributions to the strengthening. Fig. 12 also suggests that the smallest beams are near the approximate threshold for source-limited strengthening, although that threshold is only correct in an average sense and accuracy in identifying slip band spacing for small beam sizes is limited because of the increased scatter in the response. Furthermore, it can be observed that the rate of change of slip plane spacing with beam size is independent of source density, and that the average slip plane spacing for a given beam size is larger for smaller source densities.

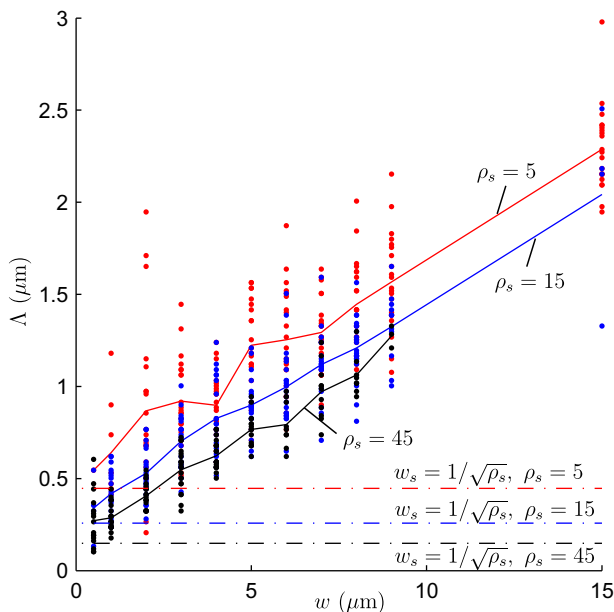


Fig. 12. Slip band spacing as a function of beam size for three different source densities.

### 5.3. Flow stress

The flow stress,  $\sigma_f$ , defined as the mean value of  $\sigma$  from the first dipole nucleation at zero plastic strain  $\varepsilon_p = 0$  up to the end of the simulation,  $\varepsilon = 0.01$ , is plotted against normalised beam size  $w/w_s$  in Fig. 13, where  $w_s$  is a length in  $\mu\text{m}$ . Once again, a total of 63 simulations were performed with different source structures for each beam size (21 for each of the three source densities). The data points correspond to  $w_s = 1/\sqrt{\rho_s}$ , and the solid lines are the average value fits to the respective data point sets. The dashed lines are the average value fits to data points corresponding to  $w_s = 1 \mu\text{m}$  (not pictured), the normalisation used in previous experimental studies. There is a strong dependence of the micro-cantilever size effect on source density for sufficiently small beams ( $w \leq 10 \mu\text{m}$ ) when  $w_s = 1 \mu\text{m}$  is used; e.g.  $\sigma_f$  is approximately 50% greater for  $w/w_s = 5$  for  $\rho_s = 5 \mu\text{m}^{-2}$  than it is for  $\rho_s = 45 \mu\text{m}^{-2}$ . The dashed lines show that the source densities considered do not have an effect on  $\sigma_f$  for large beams ( $w \geq 15 \mu\text{m}$ ), i.e. it is the value of  $1/\sqrt{\rho_s}$  relative to  $w$  that determines source limitation; increasing source density is equivalent to increasing beam size with respect to the source limitation effect. Also, for a given beam size (e.g.  $w = 5 \mu\text{m}$ ), increasing the source density beyond a threshold (e.g.  $\rho_s = 45 \mu\text{m}^{-2}$ ) has little effect for the plastic strain levels considered, i.e. source limitation is eliminated for a large enough source density for a particular plastic strain. The average value fits collapse onto a single curve for  $w_s = 1/\sqrt{\rho_s}$  (solid lines), hence the effect of source density is eliminated from the trend by this choice of normalisation.

The data points in the inset in Fig. 13 are the average values of flow stress,  $\langle \sigma_f \rangle$ , for each of the sets of 21 simulations for each beam size and source density plotted against  $(w/w_s)^{-n}$ . A least squares fit of Eq. (2) to the data points is given by the straight line, and it was found that  $A = 792 \text{ MPa}$ ,  $\sigma_0 = 133 \text{ MPa}$  and  $n = 0.89$  minimised the

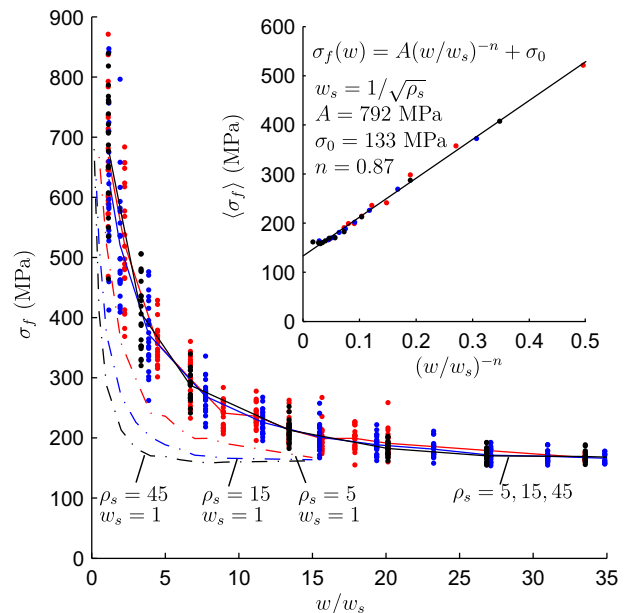


Fig. 13. The average flow stress as a function of  $w/w_s$  for  $\rho_s = 5 \mu\text{m}^{-2}$  (red),  $\rho_s = 15 \mu\text{m}^{-2}$  (blue) and  $\rho_s = 45 \mu\text{m}^{-2}$  (black) with  $w_s = 1/\sqrt{\rho_s}$  (solid line) and  $w_s = 1$  (dashed line). (For interpretation of the references to colour in this figure legend, the reader is referred to the web version of this article.)

error. The value  $\sigma_0 = 133$  MPa represents the size-independent limit. This is consistent with the experimental flow stress of the largest (10  $\mu\text{m}$ ) Ti beam shown in Fig. 5, considering that 10  $\mu\text{m}$  is near but not at the size-independent limit according to the flow stress trend evident in Fig. 5, and the simulation results of Fig. 13 which suggest the size-independent limit is approximately 15  $\mu\text{m}$ . Omitting the size-independent flow stress as done in prior experimental studies, i.e. fitting Eq. (1) to the data, leads to a considerable underestimation of  $n$  ( $\approx 0.4$ ).

#### 5.4. Yield point

Yield point increase with decreasing beam size was found to be caused by the nature of the inhomogeneity of the stress field in cantilever bending and the statistics of the source population. The most highly stressed regions in the cantilever are at the fixed end at the free surfaces, where the stress is  $\sigma^{\text{sim}}$  given by Eq. (13). The area enclosed by the  $\tau = \tau_{\text{nuc}}$  isocontour, where  $\tau_{\text{nuc}}$  is the average source strength, and the free surface of the beam is the activation area  $A_{\text{nuc}}$  over which the resolved shear stress is greater than the average source strength. This can be estimated using simple beam theory to be:

$$A_{\text{nuc}} = Lw \frac{2\tau_{\text{nuc}}}{\sigma^{\text{sim}}} \ln \left( \frac{2\tau_{\text{nuc}}}{\sigma^{\text{sim}}} \right). \quad (16)$$

Although the area fraction  $A_{\text{nuc}}/(Lw)$  is independent of beam size for fixed  $\sigma^{\text{sim}}$ , the average number of sources within the activation area,  $\rho_s A_{\text{nuc}}$ , decreases quadratically with decreasing beam size. The probability that a source strength taken from a normal distribution will be less than the average is 1/2 regardless of beam size. The probability of having a source strength lower than the average in  $A_{\text{nuc}}$  is  $\rho_s A_{\text{nuc}}/2$ . Assuming the stress throughout  $A_{\text{nuc}}$  is  $\tau_{\text{nuc}}$  for simplicity, the probability of activating a source in  $A_{\text{nuc}}$  is also  $\rho_s A_{\text{nuc}}/2$ . Hence by this reasoning the highly localised nature of the stress field in cantilever bending combined with the statistics of the source population imply that the yield point, as well as the scatter in the yield point, should increase with decreasing beam size; in pure bending  $A_{\text{nuc}}$  spans  $L$ , and in uniaxial tension  $A_{\text{nuc}}$  is  $Lw$ , hence the effect in those cases is correspondingly smaller.

## 6. Conclusions

A planar discrete dislocation plasticity (DDP) model was used to simulate micro-cantilever bending for hcp single crystals oriented for plane strain  $\langle a \rangle$  prismatic slip. The source density, standard deviation of source strength and drag coefficient were fitted to the experimental results for the largest Ti beam (regarded as the size-independent limit) and these values were used throughout; no other fitting was performed. New micro-cantilever data for Zr were reported, and the response of the beams predicted by the DDP model agreed well with the experiments for both Ti and Zr for all beam sizes. The single planar slip response of the materials studied experimentally, along with the plane strain geometry and the small length scale in bending that leads to GND structures dominating behaviour allow a 2D DDP formulation to be adopted here. An advantage of the reduced complexity of 2D simulations is that a larger number of simulations can be performed allowing the parameter space to be investigated and trends extracted.

However, care must be taken when drawing general conclusions as 3D mechanisms such as junction formation and cross slip are not incorporated.

The mechanisms of the micro-cantilever size effect were studied using the DDP model. The soft pile-up interpretation was reconciled with the geometrically necessary dislocation interpretation, noting that the former takes into account the effect of source structure. It was found that:

- Pure bending interpretations of the micro-cantilever size effect do not reveal its full behaviour. The inhomogeneous, highly localised stresses in cantilever bending influence the strengthening mechanisms and greatly enhance the influence of statistical variations in the source population on yield and flow.
- The neutral axis is not the location of soft pile-ups. Rather, soft pile-ups occur at isolines of zero resolved shear stress, which can be significantly different from the neutral axis for crystals oriented for single slip. If dislocation motion is not impeded by obstacles then this would also be observed in macroscale experiments.
- Geometrical necessity and source limitation combine to produce the observed size effect, with the latter contributing at least an equal share for very small beam sizes, such as those used in the experiments; the source density defines the minimum slip band spacing in an average sense,  $w_s = 1/\sqrt{\rho_s}$ .
- Dislocation-free regions at the free surfaces, which are independent of beam size and depend only on the source density, also contribute to the observed size effect by decreasing the plastic area fraction for smaller beams.
- Increase in the yield point and its scatter with decreasing beam size is controlled primarily by the inhomogeneous and highly localised nature of the stresses in cantilever bending, and the statistics of the source structure.
- An improved scaling law relative to that used in prior experiments was demonstrated that includes a dependence on the size-independent limit and eliminates the effect of source density from the strengthening trend by incorporating a  $w_s = 1/\sqrt{\rho_s}$  normalisation. Excluding the size-independent limit leads to a considerable underestimation of the size scaling exponent (prior studies found  $n \approx 0.5$  using Eq. (1)).
- A very large set of discrete dislocation plasticity simulations calibrated by experimental data was carried out to determine that a scaling exponent of  $n \approx 1$  fits Eq. (2) to the simulated micro-cantilever flow stress values. This exponent is independent of source density.

## Acknowledgment

We thank EPSRC for funding this research under grants EP/H018921/1, EP/G004676/1, EP/K039237/1.

## Appendix A. Dislocations exiting a concave domain

Dislocations can exit the domain along  $\Gamma_i$ , and in doing so leave behind displacement steps of  $\pm b/2$ . In order to capture the effect of this on displacement boundaries during the simulation, and the entire domain in post-processing, an exiting dislocation is kept in the simulation but treated as though it has continued to move out to infinity along its slip plane. Only its  $\tilde{u}_1$  field is used;  $\tilde{u}_2$  and the stress fields

are zeroed (all with respect to the dislocation's coordinate system). In the dislocation's coordinate system (see Fig. 1):

$$\tilde{u}_1 = \frac{b}{2\pi(1-\nu)} \left( \frac{1}{2} \frac{xy}{x^2 + y^2} - (1-\nu) \tan^{-1} \frac{x}{y} \right) \quad (\text{A.1})$$

where  $x = x_{\text{node}} - x_{\text{dis}}$  and  $y = y_{\text{node}} - y_{\text{dis}}$  are measured from the dislocation at  $(x_{\text{dis}}, y_{\text{dis}})$  to the node at  $(x_{\text{node}}, y_{\text{node}})$ . The inverse tangent term in  $\tilde{u}_1$  produces the steps since  $\tilde{u}_1(\pm\infty, y) = \mp(b/4)\text{sgn}(y)$  for finite  $y$ , and since every dislocation is part of a dipole the total step is  $\pm b/2$  either side of the slip plane. For a convex domain there is not a problem in moving dislocations out to infinity to capture exiting events. However, if a dislocation dipole in region 1 has one of the dislocations in the pair exit through the lower free surface, which is captured by  $x_{\text{dis}} \rightarrow -\infty$ , that dislocation passes through region 2 as shown in Fig. A.14(a). This would generate fictitious steps on the region 2 boundary if left uncorrected. Consequently, for a concave domain, in order to correctly calculate  $\tilde{u}$  produced by a dipole which has partially or completely exited, region 3 must follow region 2 via their shared interface:

$$\tilde{u}_1(x_1, x_2 < 0) = \tilde{u}_1(x_1, 0) \quad (\text{A.2})$$

Similarly, if a dipole is nucleated in region 2 and one of the dislocations in the pair exits the right side of the base, which is captured by  $x_{\text{dis}} \rightarrow \infty$ , that dislocation passes through region 1 as shown in Fig. A.14(b), hence the required correction is that region 3 must follow region 1 via their shared interface:

$$\tilde{u}_1(x_1 > 0, x_2) = \tilde{u}_1(0, x_2). \quad (\text{A.3})$$

Displacement information is communicated to region 2 via the line  $x_2 = 0$  and to region 1 via the line  $x_1 = 0$ . For a dipole in region 3 the domain appears convex, hence  $\tilde{u}_1$  can be evaluated for that region without correction. If the

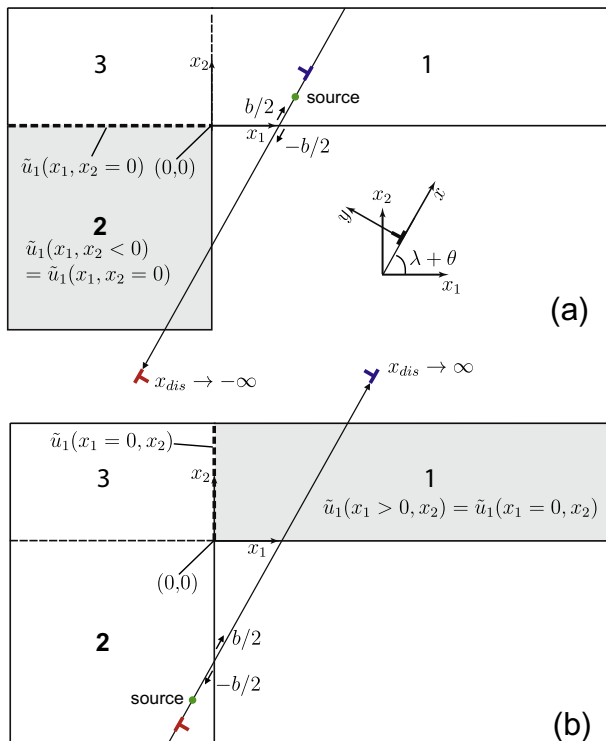


Fig. A.14. Modification of the displacement boundary conditions for dislocations exiting a concave domain.

boundary conditions are not modified in this manner, artificial slip steps form when a slip plane intersects more than two free surfaces which produces an artificial  $\hat{\sigma}$ .

## References

- [1] L. Kubin, Dislocations, Mesoscale Simulations and Plastic Flow, first ed., Oxford University Press, Oxford, 2013.
- [2] S. Rao, D. Dimiduk, T. Parthasarathy, M. Uchic, M. Tang, C. Woodward, Acta Mater. 56 (2008) 3245.
- [3] D. Norfleet, D. Dimiduk, S. Polasik, M. Uchic, M. Mills, Acta Mater. 56 (2008) 2988.
- [4] D. Balint, V. Deshpande, A. Needleman, E. Van der Giessen, Model. Simul. Mater. Sci. 14 (2006) 409.
- [5] J. Greer, W. Nix, Phys. Rev. B – Condens. Matter Mater. Phys. 73 (2006).
- [6] D. Dunstan, A. Bushby, Int. J. Plast. 53 (2014) 56.
- [7] D. Dimiduk, M. Uchic, T. Parthasarathy, Acta Mater. 53 (2005) 4065.
- [8] J. Greer, W. Oliver, W. Nix, Acta Mater. 53 (2005) 1821.
- [9] C. Volkert, E. Lilleodden, Philos. Mag. 86 (2006) 5567.
- [10] D. Kiener, C. Motz, T. Schöbert, M. Jenko, G. Dehm, Adv. Eng. Mater. 8 (2006) 1119.
- [11] J.Y. Kim, J. Greer, Appl. Phys. Lett. 93 (2008).
- [12] A. Schneider, B. Clark, C. Frick, P. Gruber, E. Arzt, Mater. Sci. Eng. A 508 (2009) 241.
- [13] A. Schneider, D. Kaufmann, B. Clark, C. Frick, P. Gruber, R. Mönig, O. Kraft, E. Arzt, Phys. Rev. Lett. 103 (2009).
- [14] Q. Sun, Q. Guo, X. Yao, L. Xiao, J. Greer, J. Sun, Scr. Mater. 65 (2011) 473, Cited By (since 1996) 18.
- [15] J. Ye, R. Mishra, A. Sachdev, A. Minor, Scr. Mater. 64 (2011) 292.
- [16] C. Byer, K. Ramesh, Acta Mater. 61 (2013) 3808.
- [17] H. Tang, K. Schwarz, H. Espinosa, Acta Mater. 55 (2007) 1607.
- [18] S. Korte, W. Clegg, Philos. Mag. 91 (2011) 1150, Cited By (since 1996) 26.
- [19] D. Dunstan, A. Bushby, Int. J. Plast. 40 (2013) 152.
- [20] M. Uchic, P. Shade, D. Dimiduk, Annu. Rev. Mater. Res. 39 (2009) 361.
- [21] O. Kraft, P. Gruber, R. Mönig, D. Weygand, Annu. Rev. Mater. Res. 40 (2010) 293.
- [22] J. Greer, J. De Hosson, Prog. Mater. Sci. 56 (2011) 654.
- [23] S. Rao, D. Dimiduk, T. Parthasarathy, M. Uchic, M. Tang, C. Woodward, Acta Mater. 56 (2008) 3245.
- [24] R. Madec, B. Devincere, L. Kubin, Phys. Rev. Lett. 89 (2002) 255508/1.
- [25] V. Bulatov, L. Hsiung, M. Tang, A. Arsenlis, M. Bartelt, W. Cai, J. Florando, M. Hiratani, M. Rhee, G. Hommes, T. Pierce, T. De La Rubia, Nature 440 (2006) 1174.
- [26] J. Senger, D. Weygand, P. Gumbsch, O. Kraft, Scr. Mater. 58 (2008) 587.
- [27] S. Rao, D. Dimiduk, M. Tang, T. Parthasarathy, M. Uchic, C. Woodward, Philos. Mag. 87 (2007) 4777.
- [28] S. Lee, S. Han, W. Nix, Acta Mater. 57 (2009) 4404.
- [29] D. Balint, V. Deshpande, A. Needleman, E. Van der Giessen, Int. J. Plast. 24 (2008) 2149.
- [30] C. Weinberger, W. Cai, Scr. Mater. 64 (2011) 529.
- [31] C. Zhou, I. Beyerlein, R. Lesar, Acta Mater. 59 (2011) 7673.
- [32] V. Deshpande, A. Needleman, E.V. der Giessen, J. Mech. Phys. Solids 53 (2005) 2661.
- [33] A. Benzerga, N. Shaver, Scr. Mater. 54 (2006) 1937.
- [34] P. Guruprasad, A. Benzerga, J. Mech. Phys. Solids 56 (2008) 132.
- [35] D. Kiener, P. Guruprasad, S. Keralavarma, G. Dehm, A. Benzerga, Acta Mater. 59 (2011) 3825.
- [36] N. Fleck, G. Muller, M. Ashby, J. Hutchinson, Acta Metall. Mater. 42 (1994) 475.
- [37] W. Nix, H. Gao, J. Mech. Phys. Solids 46 (1998) 411.
- [38] J. Stölken, A. Evans, Acta Mater. 46 (1998) 5109.

- [39] C. Motz, D. Weygand, J. Senger, P. Gumbsch, *Acta Mater.* 56 (2008) 1942.
- [40] H. Cleveringa, E. Van der Giessen, A. Needleman, *Int. J. Plast.* 15 (1999) 837.
- [41] E. Van der Giessen, A. Needleman, *Model. Simul. Mater. Sci* 3 (1995) 689.
- [42] V. Lubarda, J. Blume, A. Needleman, *Acta Metall. Mater.* 41 (1993) 625.
- [43] J. Gong, A. Wilkinson, *Acta Mater.* 59 (2011) 5970.
- [44] J. Nye, *Acta Metall. Mater.* 1 (1953) 153.
- [45] M. Ashby, *Philos. Mag.* 21 (1970) 399.